Acta Crystallographica Section A
Foundations of Crystallography
ISSN 0108-7673

Received 3 April 2006
Accepted 29 June 2006

Contributions to the application of the transferability principle and the multipolar modeling of H atoms: electron-density study of L-histidinium dihydrogen orthophosphate orthophosphoric acid. I

Ignasi Mata,[a] Enrique Espinosa,[b,e]* Elies Molins,[a] Sabino Veintemillas,[c] Waldemar Maniukiewicz,[d] Claude Lecomte,[e] Alain Cousson[f] and Werner Paulus[g]

[a]Institut de Ciència de Materials de Barcelona (CSIC), Campus UAB, 08193 Bellaterra, Spain, [b]Laboratoire d'Ingénierie Moléculaire pour la Séparation et les Applications des Gaz, LIMSAG, UMR 5633, Faculté des Sciences Gabriel, Université de Bourgogne, 6, Boulevard Gabriel, 2110 Dijon, France, [c]Instituto de Ciencia de Materiales de Madrid (CSIC), Cantoblanco, 28049 Madrid, Spain, [d]Institute of General and Ecological Chemistry, Technical University of Łódź, 90-924 Łódź, ul. Żwirki, 36, Poland, [e]Laboratoire de Cristallographie et Modélisation des Matériaux Minéraux et Biologiques, LCM^{3}B, UMR CNRS 7036, Faculté des Sciences, Université Henri Poincaré, Nancy I, BP 239, 54506 Vandoeuvre-lès-Nancy CEDEX, France, [f]Laboratoire Léon Brillouin, CEA-CNRS, CEA-Saclay, 91191 Gif-sur-Yvette CEDEX, France, and [g]Laboratoire de Chimie du Solide et Inorganique Moléculaire, UMR 6511, Université de Rennes 1, Campus Beaulieu, Avenue Général Leclerc, 35042 Rennes CEDEX, France. Correspondence e-mail: enrique.espinosa@lcm3b.uhp-nancy.fr

The electron density of L-histidinium dihydrogen orthophosphate orthophosphoric acid has been determined from X-ray and neutron diffraction data at low temperature (120 K). Topological analysis of the electron density has been used to analyse the effect of the multipolar refinement strategy on the electron-density model in the hydrogen-bonding regions. The electron density at low temperature has also been used to acquire high-quality experimental thermal parameters at room temperature using the transferability principle. Molecular vibrations, TLS and normal mode analysis are discussed and studied at both temperatures.

1. Introduction

In the last few years, X-ray high-resolution diffraction data have been used to study the crystalline electron distribution $\rho(\mathbf{r})$ of a large diversity of materials (Koritsanszky & Coppens, 2001; Lecomte *et al.*, 2005). Some of these studies have been performed on materials exhibiting non-linear optical (NLO) properties, with the aim to explore the relationship between these properties and $\rho(\mathbf{r})$. These materials included phosphate salts with an organic cation. The efficiency of these organic phosphates for second-harmonic generation is far from that of purely organic crystals but they offer a good compromise between the physical properties required for applications (Masse & Zyss, 1991; Yokotani *et al.*, 1989). Therefore, they are potential substitutes for materials widely used today (Eimerl *et al.*, 1989). For this reason, electron-density distributions of some of these compounds have been determined (Espinosa *et al.*, 1996; Puig-Molina *et al.*, 1998). The crystal structure of L-histidinium dihydrogen orthophosphate orthophosphoric acid (LHP) (Fig. 1) described for the first time by Blessing (1986) belongs to the phosphate salts family with potential NLO properties.

The crystal structure of LHP (monoclinic, $P2_1$) shows the phosphate anions and the phosphoric acid molecules forming layers parallel to the (100) plane (Fig. 2). These layers are built by successive columns of $H_2PO_4^-$ and H_3PO_4 molecules running along the 2_1 axes. The cations are sandwiched between the planes. All these molecules are joined by a complex network of hydrogen bonds, some of them presenting very short donor–acceptor distances.

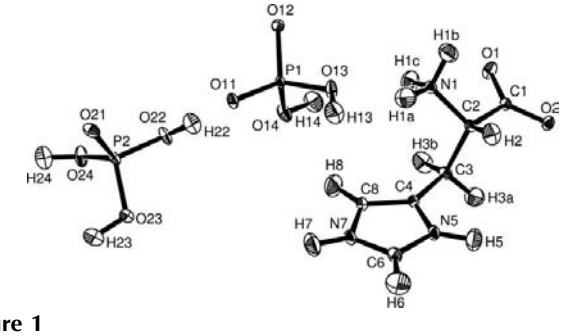

Figure 1
ORTEP view (Johnson, 1965; Farrugia, 1997) of LHP from the XL-Nb refinement. Ellipsoids are set to the 50% probability level.

The main aim of this work concerns the treatment of H atoms in the experimental determination of the electron-density distribution from X-ray and neutron diffraction data. This has been monitored by using the topological analysis of $\rho(\mathbf{r})$ (Bader, 1990) in intermolecular regions, where hydrogen-bonding interactions take place. The electron-density distribution observed in the intramolecular regions of LHP will be described elsewhere in the second part of this series, where the effect of crystal environment on the electron-density distribution of the molecules will be analysed and compared with the aid of *ab initio* calculations. On the other hand, a further methodological question approached in this work is connected with the application of the transferability principle (Pichon-Pesme *et al.*, 1995) to the improvement of the quality of the atomic anisotropic displacement parameters (ADP's) by using the $\rho(\mathbf{r})$ multipolar model, fitted against the X-ray structure factors.

The hydrogen-bonding network in LHP covers a large variety of contacts, from very strong O$\cdots$O to weak C$\cdots$O interactions, spread in a wide range of donor–acceptor distances. The quality of the $\rho(\mathbf{r})$ modeling in intermolecular regions can be tested by comparing experimental and theoretical results on the properties of the observed electron-density distribution in hydrogen bonds (Espinosa, Souhassou *et al.*, 1999; Espinosa & Molins, 2000; Espinosa *et al.*, 2002). According to these works, topological properties of $\rho(\mathbf{r})$ in hydrogen-bonding regions show continuous dependences on the H$\cdots A$ distance, presenting different regimes depending on the nature of the interaction.

2. Experimental

2.1. Crystal growth

Small LHP crystals were obtained by slow absorption of ethanol at room temperature. The starting solution was prepared by dissolving 60 g (0.387 mol) of L-histidine (Riedel-de Häen, Blosinth Reagent) and 89.16 g (0.774 mol) of H_3PO_4 85% $d = 1.7$ g cm^{-3} (Merck, Analytical Reagent) in 200 cm^3 of distilled water. This solution, seeded with a few milligrams of solid LHP, was introduced in a vacuum desiccator over two litres of ethanol 90% (1800 cm^3 absolute ethanol Carlo Erba Codex Reagent and 200 cm^3 of distilled water). After 13 d, 129 g of thin elongated crystals of LHP were obtained. The yield of the process was 95.2%.

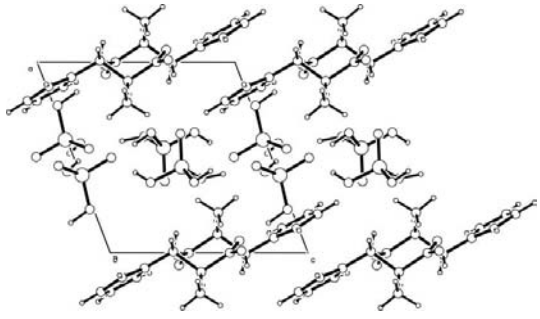

Figure 2
Projection view of the LHP structure along **b**.

For the neutron experiment, larger crystals of LHP were grown from a solution prepared by dissolving LHP crystals in distilled water up to saturation at room temperature (32.4%). 224 g of this solution were introduced into a cylindrical recipient provided with four horizontal separation discs, seeded and left half closed in a vacuum desiccator over 1355 g of ethanol 84% (Carlo Erba, Codex Reagent). Vacuum was made in the desiccator until the ethanol started to boil. After 169 d, approximately 35 g of ethanol were absorbed by the LHP solution and 7 g of water passed from the LHP solution to the hydroalcoholic solution. The obtained crystals were elongated and of centimetric size.

2.2. X-ray diffraction experiment

Two single-crystal X-ray diffraction experiments were performed, one at room temperature (hereafter XR experiment) and the other using a nitrogen jet-stream low-temperature system (hereafter XL experiment). In both cases, the selected specimens showed high crystalline quality. Both experiments were performed on an Enraf–Nonius CAD4 diffractometer equipped with graphite monochromator and Mo $K\alpha$ radiation.

In the XL experiment, the temperature of the crystal was fixed at 120 (3) K, according to a calibration using the paraferroelectric KDP transition at 123 K. Before cooling the crystal, a set of reflections was measured at room temperature and used in a previous structure determination in order to check the quality of the crystal. All reflections in the Ewald sphere were collected up to 0.90 Å^{-1} in XL and up to 0.96 Å^{-1} in XR. For XR, 79% of the reflections with $\sin(\theta)/\lambda > 0.90$ Å^{-1} were not significant [only 44% non-significant reflections in the interval $0.90 < \sin(\theta)/\lambda < 0.96$ Å^{-1} for the XL experiment]. For XL, half a sphere with $\sin(\theta)/\lambda < 0.60$ Å^{-1} was again measured in order to get a larger number of equivalent reflections in the low-angle data set. For higher $\sin(\theta)/\lambda$ data, only selected reflections with expected significant intensities were measured. Owing to this data-collection strategy, the XL and XR data sets exhibit an overall completeness of 55 and 42%, respectively. These low values contrast with those usually obtained with bidimensional CCD detectors. However, $I_{\rm Bragg}$ integrations and $R_{\rm int}$ values corresponding to high-order reflections measured with two-dimensional detectors do not always show better results than those obtained with old-fashioned data-collection strategies and one-dimensional detectors, and often lead to scale-factor problems between high-order and low-order reflections (Kuntzinger *et al.*, 1999).

Data were collected in the $\omega/2\theta$ profile mode. The prescan speed and the largest measuring time for a single reflection were 16.5° min^{-1} and 100 s for XL and 5.5° min^{-1} and 120 s for XR, respectively. Data reduction was performed using the *DREADD* package (Blessing, 1987, 1989). Once the background was subtracted and the Lorentz and polarization corrections performed, the intensities were integrated. Decay

Table 1
Crystal parameters and data-collection details.

	XR	XL	NR	NL
Chemical formula	$C_6H_{15}N_3O_{10}P_2$			
Crystal system	Monoclinic			
Space group	$P2_1$			
Radiation	X-rays	X-rays	Neutrons	Neutrons
λ (Å)	0.71073	0.71073	0.8308	0.8308
Temperature (K)	294 (1)	120 (3)	293 (2)	120 (5)
Crystal dimensions (mm)	0.50 × 0.30 × 0.20	0.45 × 0.35 × 0.32	6 × 3 × 2	6 × 3 × 2
Reflections for cell determination	25	25	16	18
θ interval	$12 < \theta < 19^\circ$	$12 < \theta < 29^\circ$	$11 < \theta < 17^\circ$	$16 < \theta < 25^\circ$
Cell parameters				
a (Å)	9.155 (2)	9.084 (3)	9.15 (1)	9.037 (6)
b (Å)	8.913 (1)	8.913 (1)	8.91 (1)	8.906 (5)
c (Å)	8.806 (2)	8.786 (2)	8.81 (1)	8.759 (5)
β (°)	111.35 (2)	111.03 (9)	111.4 (5)	110.93 (9)
V (Å^3)	669.2 (2)	664.0 (3)	669 (3)	658.4 (8)
Scan type	$\omega/2\theta$	$\omega/2\theta$	$\omega/2\theta$	ω
Measured reflections	24122	27602	4982	4475
Unique reflections (R_{int})	5860 (0.059)	7634 (0.027)	3535 (0.039)	3423 (0.087)
Miller indices	$-22 \le h \le 22$	$-22 \le h \le 22$	$-13 \le h \le 15$	$-15 \le h \le 15$
	$-19 \le k \le 19$	$-23 \le k \le 23$	$-15 \le k \le 0$	$-15 \le k \le 0$
	$-17 \le l \le 20$	$-16 \le l \le 22$	$-14 \le l \le 6$	$-14 \le l \le 8$
$[\sin(\theta)/\lambda]_{max}$ (Å^{-1})	1.35	1.35	0.85	0.88
Standard reflections	611	$\bar{2}5\bar{2}$	200	200
	$73\bar{4}$	$73\bar{4}$	002	002
	502	313		
Absorption coefficient (mm^{-1})	0.372	0.374		
Total exposition time (h)	669	687	648	720

effects were corrected by a third-degree polynomial function fitted to the standard reflection intensities, which were measured at intervals of 2 h in XL and of 1 h in XR. The instrumental instabilities (McCandlish *et al.*, 1975) were 0.013 for XL and 0.027 for XR. Absorption correction was performed by means of a Gaussian numerical quadrature using the *ABSORB* program (DeTitta, 1985), obtaining maximum and minimum transmission factors of 0.923 and 0.886 for XL and 0.938 and 0.870 for XR, respectively.

The set of measured reflections (27602 for XL and 24122 for XR) were merged with *SORTAV* obtaining the unique reflections (7762 with R_{int} = 0.024 for XL and 5860 with R_{int} = 0.059 for XR). In order to correct for anomalous scattering, the XL data-set reflections were merged again treating Friedel pairs as independent (14311 unique reflections with R_{int} = 0.021). Then, after anomalous-scattering correction (see §3.2.2), Friedel pairs were merged (7634 unique reflections with R_{int} = 0.027). More information about the data collections and reductions can be found in Table 1.

2.3. Neutron diffraction experiment

Two single-crystal neutron diffraction experiments were also performed, one at room temperature (hereafter NR experiment) and the other at low temperature (hereafter NL experiment). Both were performed on a Stoe four-circle diffractometer mounted at a hot neutron line in the ORPHEE reactor and equipped with a copper monochromator. The low-temperature system used in the NL experiment consisted of a sealed chamber containing the crystal with cold helium circulation.

The same LHP specimen was used in both experiments. Reflections were measured as profiles, from which the intensities were obtained after subtracting the background and correcting for the Lorentz effect. Decay and absorption corrections were not performed as the corresponding effects were not detected. Finally, equivalent reflections were merged. More information about data collections and reductions can be found in Table 1.[1]

3. Least-squares refinement

Four crystal structures and one electron-density distribution were obtained from the four sets of diffraction data. Crystal structures at low and room temperatures were obtained from neutron diffraction data. The electron-density distribution was obtained from a refinement against low-temperature data which included crystal-structure information from the neutron data. The parameters describing the electron-density distribution were used to enhance the quality of the crystal-structure determination against the X-ray data at room temperature (Pichon-Pesme *et al.*, 1995). The four final models were preceded by previous refinements as explained in detail in the following sections. Finally, four thermal vibration models were obtained from TLS refinements (Schomaker & Trueblood, 1968; Dunitz *et al.*, 1988) against structural data from the four final models.

3.1. Refinement against neutron data

The structure refinements were performed against both sets of neutron data (NR and NL) using the neutron scattering lengths of Sears (1992). Anisotropic displacement parameters (ADP's) were introduced for all atoms, including H atoms. In the refinement against NL data, the low-temperature X-ray unit-cell parameters were used instead of the neutron ones.

In order to correct for extinction effects, an additional parameter was introduced in the refinement against both NR and NL data sets according to the Becker–Coppens isotropic extinction model (Becker & Coppens, 1974). Type I and type II extinctions with Lorentzian or Gaussian distributions of the

[1] Supplementary data for this paper, including tables of multipolar parameters for H atoms for different refinements and of normal mode frequencies of LHP for different refinements, and residual maps, are available from the IUCr electronic archives (Reference: SH5044). Services for accessing these data are described at the back of the journal.

Table 2
Least-squares refinements against diffraction data.

The corresponding data set is specified by the first part of the refinement name. *R* refers to all the reflections in the refinements against *F*, or to the reflections with $I > 3\sigma(I)$ in the refinements against F^2. *wR* refers to the magnitude used in the refinement (*F* or F^2). z^2 is the difference of the mean squared vibration amplitudes along the bond direction of the bonded atoms (Hirshfeld, 1976) and σ is the standard uncertainty of $\langle z^2 \rangle$. $\langle z^2 \rangle$, σ and z^2_{max} are given in 10^4 Å^2.

Refinement	Reflections	Parameters	F^2/F	*R*	*wR*	GoF	$\langle z^2 \rangle$	σ	z^2_{max}
XR-HO	3814	189	F^2	0.032	0.100	0.78	5.8	3.8	13
XR-A	5860	189	F^2	0.023	0.063	0.75	5.3	4.3	14
XL-HO	2511	189	F^2	0.041	0.109	0.94	4.0	2.4	10
XL-A	6558	512	*F*	0.018	0.016	0.86	3.3	1.7	6
XL-Na	6558	605	*F*	0.017	0.016	0.84	3.2	1.9	6
XL-Nb	6558	538	*F*	0.018	0.016	0.86	3.1	1.8	6
XL-Nc	6558	553	*F*	0.018	0.016	0.85	3.1	1.8	6
NR-A	3535	325	F^2	0.028	0.058	1.06	4.7	3.1	10
NL-A	3553	325	F^2	0.050	0.125	2.24	8.1	5.7	22
NL-B	3553	325	F^2	0.035	0.076	1.81	5.2	5.3	16

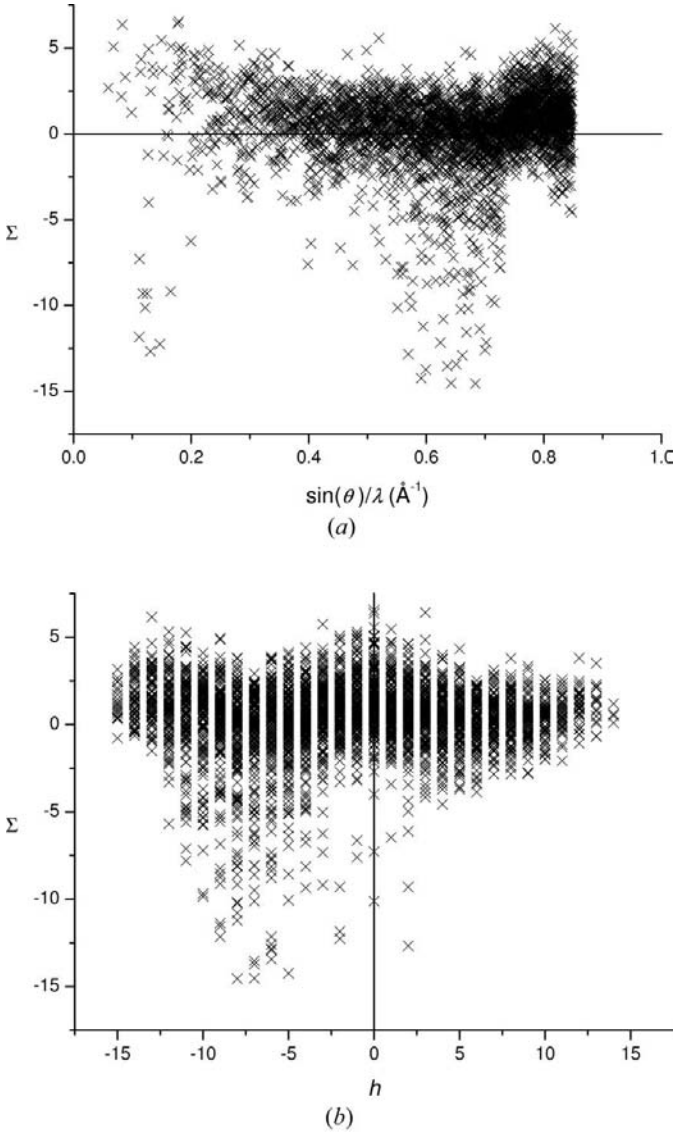

Figure 3
$\Sigma = (F^2_{calc} - F^2_{obs})/\sigma(F^2_{obs})$ values for the reflections used in the NL-A refinement *versus* (*a*) $\sin(\theta)/\lambda$ and (*b*) *h* Miller index.

crystal domains were tested in four different refinements. Slightly better agreement factors and rigid-bond test (Hirshfeld, 1976) results were obtained when using a type II extinction with Lorentzian distribution for both NL and NR data sets. Therefore, the refinements with this extinction model were retained (refinements NR-A and NL-A in Table 2). The highest extinction values (064 reflection) were $y = 0.591$ and 0.541 for NR and NL, respectively ($F^2_{obs} = yF^2_{calc}$).

According to the agreement factors and the rigid-bond test results, the NR-A refinement provides a good LHP structure and thermal vibration description, while this is not the case for the NL-A refinement. Moreover, in this refinement the mean square displacement amplitude along the bond direction was smaller for the H atom in the two *X*—H bonds, a result without physical sense.

A detailed analysis of these NL refinements reveals that the values $\Sigma = (F^2_{calc} - F^2_{obs})/\sigma(F^2_{obs})$ do not correspond to a normal error distribution. The largest Σ values are in general negative and concentrated in one region of reciprocal space [$0.50 < \sin(\theta)/\lambda < 0.70$ Å^{-1} and $h < 0$], suggesting the presence of systematic errors in the data collection and/or in the data reduction (Fig. 3).

As anisotropic extinction refinement failed, correction factors were finally obtained by fitting a transmission surface to the experimental intensities using *DIFABS* (Walker & Stuart, 1983). In a new refinement against the corrected intensities (refinement NL-B in Table 2), an improvement in both the agreement factors and the rigid-bond test is observed compared to NL-A. The abnormal behaviour exhibited by the ADP's of some H atoms also disappears in this refinement.

The average of the U_{33}(NL-A)/U_{33}(NL-B) ratios is 0.60 (13), while the analogous values for U_{11} and U_{22} are 0.98 (4) and 1.06 (8) Å^2, respectively. Therefore, it follows that the *DIFABS* correction mostly affects the atomic thermal vibration along **c**, increasing the value of U_{33}. The average of the U_{eq}(NL-A)/U_{eq}(NL-B) ratios is 0.90 (3), indicating that equivalent isotropic displacement parameters were quite affected by *DIFABS*.

As no problem was detected in the experimental set-up, and as the low-temperature experiment was performed after the room-temperature one on the same crystal, the low-temperature data quality should be due to a deterioration of the crystal quality during the cooling process.

3.2. Refinements against X-ray data

Two models were used: the independent-atoms model (IAM) and the Hansen–Coppens model (Hansen & Coppens, 1978) based on a multipolar expansion of the electron-density distribution (Stewart, 1976):

$$\rho(\mathbf{r}) = \sum_j \rho_{\rm at}(\mathbf{r} - \mathbf{r}_j), \quad (1)$$

where

$$\rho_{\rm at}(\mathbf{r}) = \rho_{\rm core}(r) + P_v\kappa^3\rho_{\rm val}(\kappa r) + \sum_{l=0}^{l_{\rm max}}\sum_{m=0}^{l}\kappa'^3 R_{nl}(\kappa' r)P_{lm\pm}y_{lm\pm}(\theta,\varphi). \quad (2)$$

In this expression, $\rho_{\rm core}(r)$ and $\rho_{\rm val}(r)$ represent respectively the free-atom core and the valence-shell electron-density distributions. $R_{nl}(r)$ is a Slater-type radial function and $y_{lm\pm}(\theta,\varphi)$ are spherical harmonic functions in real form. P_v and $P_{lm\pm}$ are the multipolar population parameters and κ and κ' are expansion–contraction coefficients.

In this study, the core scattering factors were taken from Doyle & Cowley (1974). The valence electron density was defined by the Clementi wavefunctions (Clementi & Roetti, 1974). A bound atom form factor was used for H atoms (Stewart *et al.*, 1965). The multipolar expansion was extended up to the hexadecapolar term ($l_{\rm max} = 4$) for P atoms and up to the octupolar term ($l_{\rm max} = 3$) for C, N and O atoms. In the case of H atoms, the expansion was extended up to the dipolar ($l_{\rm max} = 1$) or the quadrupolar ($l_{\rm max} = 2$) term, depending on the refinement. The radial n_l and ζ parameters were selected according to Hansen & Coppens (1978), Espinosa (1994) and Espinosa *et al.* (1996): 1, 1 and 2.25 for H; 2, 2, 3 and 3.0 for C; 2, 2, 3 and 3.8 for N; 2, 2, 3 and 4.5 for O in the carboxyl group; 1, 2, 4 and 4.5 for O in the phosphate and phosphoric acid groups, and 6, 6, 6, 6 and 3.6 bohr^{-1} for P atoms. All refinements were performed with the *MOLLY* program (Hansen & Coppens, 1978).

3.2.1. Independent-atoms model. H atoms were found by difference-Fourier synthesis and refined isotropically. Their coordinates were then shifted by extending along the X—H (X = C, N, O) bond vectors to average bond-distance values observed from neutron diffraction data [d(O—H) = 0.967, d(N—H) = 1.032, d(Csp^2—H) = 1.092, d(Csp^3—H) = 1.099, d($N_{\rm ring}$—H) = 1.009 and d($C_{\rm ring}$—H) = 1.077 Å] (Allen *et al.*, 1992). These distances were kept fixed and the isotropic thermal vibrations were set to 1.5 or 1.2 times the $U_{\rm eq}$ of the bonded atom depending on whether X was located at the terminal part of the molecule or not.

The four extinction models described in §3.1 were used in the refinement against the X-ray data, however the corresponding extinction parameter always remained smaller than its standard uncertainty. Therefore, no extinction correction was applied in the subsequent refinements.

The obtained models were used as starting point for two high-order refinements (Ruysink & Vos, 1974) in order to obtain unbiased ADP's from deformation density effects (Coppens, 1968). Only reflections exhibiting a resolution of $\sin(\theta)/\lambda > 1.0$ Å^{-1} (for XL) and 0.7 Å^{-1} (for XR) were chosen in order to satisfy the rigid-bond test (Hirshfeld, 1976). The selected cut-off values offered a sufficient ratio of observations to parameters. Agreement factors for both high-order refinements are given in Table 2 (entries XR-HO and XL-HO).

3.2.2. X–X refinement against low-temperature data. The IAM model obtained in the XL-HO refinement was used as starting point in a preliminary X–$X_{\rm HO}$ multipolar refinement against the XL data. In order to avoid as much as possible the correlation between the refined parameters, due to the $P2_1$ noncentrosymmetric space group, local symmetry conditions were applied by fixing to zero selected P_{lm} parameters according to Kurki-Suonio (1977). Thus, for non-H atoms, the constrained local symmetries were: a twofold axis at the P atom in the phosphate group, a threefold axis at the P atom belonging to the phosphoric acid group, and a mirror plane for atoms in carboxyl and imidazole groups. In the case of H atoms, only one multipolar parameter, corresponding to the dipole along the bond direction, was refined. The same κ parameter was used for chemically equivalent atoms with similar environment. All κ' parameters were kept fixed to 1 throughout the refinement because their eventual refinement produced either convergence problems or meaningless results (Pérès *et al.*, 1999).

The refinement, performed against F, was divided into four stages. Besides the scale factor, the parameters refined at each stage were: (i) P_v and κ, (ii) P_{lm}, (iii) P_v, κ and P_{lm}, and (iv) P_v, κ, P_{lm}, and positions and ADP's of non-H atoms. The convergence was achieved with $R = 0.017$ for 6558 reflections.

In order to correct F_o's for anomalous-scattering effects, the reflections for the XL experiment were merged treating the Friedel pairs as independent reflections (see §2.2) and the same refinement was performed against this new data set ($R = 0.033$); the obtained model was used for correcting the structure factors from anomalous-scattering effects (Souhassou *et al.*, 1995) using the anomalous-scattering factors from Creagh & McAuley (1992). The corrected structure factors were then merged, obtaining a new data set.

This last data set was used in a new X–$X_{\rm HO}$ refinement, using the same strategy as in §3.2.1 (refinement XL-A in Table 2). As the anomalous scattering effect is in fact small, even at high resolution where the anomalous-scattering effect is relatively large [while f decreases with increasing $\sin(\theta)/\lambda$, f' and f'' do not], both preliminary and XL-A refinements are very similar. However, a careful comparison between ADP's shows a slight improvement in the rigid-bond test when using this corrected data set. Therefore, it was used in the X–(X+N) refinements.

3.2.3. X–(X+N) refinements against low-temperature data. A tentative X–N refinement (Coppens, 1970) against XL data

was first performed, using the IAM model obtained from the NL-B refinement as starting point. However, as the ADP's obtained from the XL-HO and NL-B refinements were slightly different, probably due to (i) the temperature difference between the X-ray and neutron experiments and (ii) the different contributions derived from thermal diffuse scattering, extinction and absorption effects to both data sets; the X–N refinement was unsuccessful. X–(X+N) refinements (Coppens *et al.*, 1981) were then performed with the non-H-atom positions and ADP's taken from the XL-HO refinement and from the NL-B refinement for H atoms. The ADP's of the H atoms were scaled according to the transformation

$$U_{ij}(\text{XL-HO}) = sU_{ij}(\text{NL-B}) + \Delta U_{ij}, \qquad (3)$$

where the parameters s and ΔU_{ij} were obtained using the program *UIJXN* (Blessing, 1995*b*) [$s = 1.15\,(2)$, $\Delta U_{11} = -0.0003\,(3)$, $\Delta U_{12} = 0.0002\,(1)$, $\Delta U_{13} = -0.0021\,(1)$, $\Delta U_{22} = -0.0019\,(3)$, $\Delta U_{23} = 0.0000\,(1)$, $\Delta U_{33} = -0.0057\,(3)$, $\chi^2 = 1.31$].

The X–(X+N) refinements were performed following the same strategy described in §3.2.2, including the refinement of positions and ADP's of non-H atoms. In order to explore the best procedure to obtain the electron-density distribution around the H atoms, two X–(X+N) refinements were performed. In the first one (XL-Na refinement), the H-atom multipolar expansion was extended up to the quadrupolar term, as recommended by Chandler & Spackman (1982). In the other refinement (called XL-Nb), the multipolar expansion was truncated at the dipolar level. As seen in Table 2, both refinements give similar agreement factors in spite of the larger number of parameters in XL-Na. In the XL-Na model, only 9 of 67 parameters related to the H-atom quadrupolar terms (8 parameters were not refined owing to local symmetry conditions) had values larger than three times their standard uncertainty.

At most, one quadrupolar parameter was significant for each H atom. Moreover, the parameter was always related to charge reorganization along the axis defined by the covalent bond. It was judged that this effect would be better represented by the $y_{20}(\theta, \varphi)$ term, which is the only quadrupole with cylindrical symmetry directed along the covalent bond. Therefore, a new refinement using the P_{20} parameter only among the H-atom quadrupolar terms was performed (entry XL-Nc in Table 2).

Finally, the local atomic symmetry constraints were validated by comparing statistics-of-fit and residual difference densities from the constrained model (XL-Na) with those from a model without the constraints.

As seen in Table 2, the final X–(X+N) models obtained from the XL-Na, XL-Nb and XL-Nc refinements show an excellent deconvolution between the static electron density and the thermal vibration, according to the rigid-bond test. The residual maps (Fig. 4) show in most cases a random distribution of peaks and holes around almost all atoms and in the hydrogen-bond regions. The only important deviations from a random residual noise are located close to P atoms, where peaks larger than three times the standard uncertainty of the electron density (Cruickshank, 1949), calculated either as $\sigma = [\sum \sigma^2(F_{\rm obs})/V^2]^{1/2} \approx 0.06\,\text{e Å}^{-3}$ or as $\sigma = [\sum (F_{\rm obs} - F_{\rm calc})^2/V^2]^{1/2} \approx 0.05\,\text{e Å}^{-3}$, are observed. These peaks are also present in the residual maps calculated

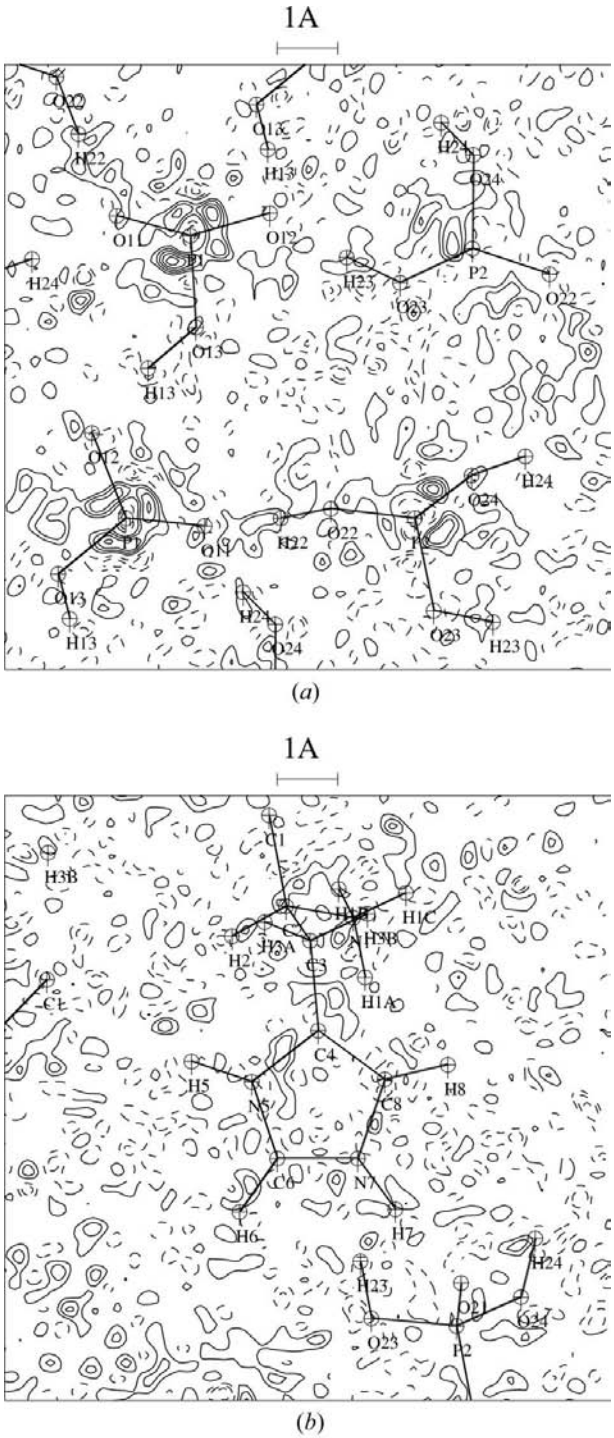

Figure 4
Residual electron-density maps for the (XL-Nb) refinement, using reflections with $I > 3\sigma(I)$, in the planes defined by atoms (*a*) P1, P2 and P1 ($1-x$, $-1/2+y$, $2-z$) and (*b*) C4, C6 and N7. Contour intervals are 0.05 e Å^{-3}. Continuous and dashed contours represent positive and negative density, respectively. The zero contour is not represented for clarity. The largest value observed in the residual maps is 0.25 e Å^{-3}.

Table 3
Agreement factors, defined as $R = \left[\sum (U_{obs} - U_{calc})^2 / \sum U_{obs}^2\right]^{1/2}$, for all the TLS refinements.

Model	Phosphate	Phosphoric acid	Histidinium (TLS)	Histidinium (TLS+$\langle\varphi\rangle$)
XL-Nb	0.023	0.019	0.142	0.132
XR-A	0.030	0.018	0.180	0.128
NL-B	0.019	0.040	0.277	0.108
NR-A	0.033	0.026	0.249	0.137

from the XL-HO refinement. All attempts to remove them by (i) relaxation of local symmetry conditions, (ii) optimization of the phosphorus radial function by testing different values of the radial function parameters (n_l = 4, 4, 4, 4, ζ = 2.4, 3.0 a_0^{-1}; n_l = 5, 5, 5, 5, ζ = 3.0, 3.6 a_0^{-1}; n_l = 6, 6, 6, 6, ζ = 3.6, 4.2 a_0^{-1}; n_l = 6, 6, 7, 7, ζ = 4.2, 4.8 a_0^{-1}; n_l = 7, 7, 7, 7, ζ = 4.2, 4.8 a_0^{-1}) (Moss *et al.*, 1995), (iii) refinement with Gram–Charlier parameters describing the anharmonic vibrations (Kuhs, 1983), (iv) additional absorption correction using the algorithm described in Blessing (1995*a*), and (v) refinements with fixed values of the scale factor were unsuccessful.

3.2.4. Multipolar refinements against room-temperature data. In order to check how the multipole parameters improve the quality of the LHP structure at room temperature, a new structural refinement (XR-A refinement) was carried out against the XR data set using the transferability principle (Pichon-Pesme *et al.*, 1995). All reflections were used and the IAM form factors were substituted by the generalized form factors obtained in XL-Nb. As the static electron-density distribution is temperature independent (in first approximation, if the shrinkage of the crystal structure at low temperature is neglected and no phase transition appears between both temperatures), the XR-*A* thermal parameters should present reduced biased effects due to the deformation electron density, even when only low-angle reflections are included in the refinement.

The comparison of XR-HO and XR-A (Table 2) reveals that the rigid-bond test is, on average, slightly better when using generalized form factors. Considering the rigid-bond test for the L-histidinium moiety, the better quality of the ADP's in the XR-A model is evident ($\langle z^2\rangle = 6.09 \times 10^{-4}$ and 4.00×10^{-4} Å^2 for XR-HO and XR-A, respectively), confirming the method used for high-resolution protein refinement (Jelsch *et al.*, 2000; Guillot *et al.*, 2001). On the other hand, the rigid-bond test applied on the P—O bonds is clearly worse for the XR-A model ($\langle z^2\rangle = 5.50 \times 10^{-4}$ and $\langle z^2\rangle = 7.25 \times 10^{-4}$ Å^2 for XR-HO and XR-A, respectively). This effect seems to be related to some residuals around the P atoms (Fig. 4), and suggests a deficiency in the multipolar model, which affects the quality of the ADP's.

3.2.5. TLS refinements. In order to study molecular vibrations in LHP, a TLS model was fitted to the atomic thermal parameters. The TLS refinements were performed with the *THMA14* program (Schomaker & Trueblood, 1998).

Four fittings were performed for each moiety (histidinium, $H_2PO_4^-$ and H_3PO_4) against the ADP sets respectively obtained from XR-A, NR-A, XL-Nb and NL-B. The suitability of the rigid-body approximation for the molecular vibrations was checked by the rigid-molecule test (Rosenfield *et al.*, 1978). In the case of histidinium, this clearly shows that the contribution of internal modes to the molecular vibration is significant. The internal vibration was treated by using a TLS + $\langle\varphi\rangle$ model, which is a generalization of the TLS model for rigid-body vibrations. For this model, additional parameters were introduced in the TLS refinement in order to describe the relative movement of a set of atoms, called attached rigid group (ARG), with regard to the rest of the atoms in the molecule (Trueblood & Dunitz, 1983; Bürgi, 1989).

In the TLS + $\langle\varphi\rangle$ refinements, imidazolyl and carboxylate were treated as molecular body and ARG, respectively. The relative movement of both groups was defined as the variation of one of the torsion angles of the O1—C1—C2—C3—C4—C8 chain (Fig. 1). Only one of these angles could be varied at each time, as riding groups must be attached to the molecule body. The best agreement factors were obtained taking as internal vibration the variation of the O1—C1—C2—C3 torsion angle. The final agreement factors for TLS and TLS + $\langle\varphi\rangle$ refinements are given in Table 3.

4. Results and discussion

4.1. Hydrogen-bonding network

The crystal structures (Fig. 1) observed at both temperatures are very close to each other, exhibiting very similar hydrogen-bonding geometries in all the models (Table 4). Two weak C—H···O interactions not previously reported (Blessing, 1986) were found thanks to the topological analysis of the electron-density distribution (§4.3). The crystal packing is shown in Fig. 2.

In the LHP structure, the hydrogen-bond network binding the different moieties comprises 12 intermolecular interactions, with H···O distances ranging from 1.420 to 2.381 Å. The five strongest O—H···O hydrogen bonds [1.420 < d(H···O) < 1.597 Å] involve phosphate anions as either donors or acceptors. The strongest interaction (O13—H13···O12) is between neighbouring phosphates related *via* a 2_1 symmetry element. This anion acts as an acceptor in three strong interactions with phosphoric acid molecules and as a donor in another O—H···O hydrogen bond with the histidinium carboxyl group. There are also weaker N—H···O interactions [1.676 < d(H···O) < 2.038 Å] joining the cations to each other and to the $H_3PO_4 \cdot H_2PO_4^-$ layers. In all the hydrogen bonds, except for two of the three weakest interactions, the X—H distance, as derived from the neutron diffraction experiment, is larger than the average neutron diffraction distance according to Allen *et al.* (1992) (Table 4).

Special attention is needed for atom H13, which is involved in the strongest intermolecular interaction [d(H···O) = 1.420 (1) Å]. In this case, the O···O distance [d(O···O) = 2.468 (2) Å] is only slightly larger than those observed in the symmetric O—H—O bonds in methylammonium salts (Flensburg *et al.*, 1995; Madsen *et al.*, 1998), exhibiting O···O

Table 4
Hydrogen-bond distances and angles in LHP according to (first line) XL-Nb and to (second line) XR-A refinements.

	$X\cdots$O (Å)	X—H (Å)	H$\cdots$O (Å)	$\widehat{\text{XHO}}$ (°)
O13—H13$\cdots$O12($1-x,-1/2+y,2-z$)	2.468 (2)	1.056 (1)	1.420 (1)	170.74 (6)
	2.461 (1)	0.967	1.505 (2)	171.0 (1)
O22—H22$\cdots$O11	2.546 (1)	1.025 (1)	1.522 (1)	175.85 (7)
	2.548 (1)	0.967	1.578 (1)	178.9 (1)
O14—H14$\cdots$O2($2-x,1/2+y,3-z$)	2.561 (1)	1.035 (1)	1.530 (1)	172.76 (8)
	2.568 (1)	0.967	1.603 (1)	172.5 (1)
O23—H23$\cdots$O12($x,y,-1+z$)	2.569 (1)	1.014 (1)	1.558 (1)	174.19 (8)
	2.580 (1)	0.967	1.613 (1)	174.8 (3)
O24—H24$\cdots$O11($1-x,1/2+y,1-z$)	2.583 (1)	1.035 (1)	1.597 (1)	168.34 (9)
	2.584 (1)	0.967	1.623 (1)	170.5 (1)
N5—H5$\cdots$O1($2-x,-1/2+y,3-z$)	2.653 (1)	1.051 (1)	1.676 (1)	152.42 (4)
	2.656 (1)	1.009	1.713 (1)	153.7 (1)
N7—H7$\cdots$O21($1-x,-1/2+y,1-z$)	2.718 (1)	1.048 (1)	1.679 (1)	170.47 (5)
	2.726 (1)	1.009	1.723 (1)	171.7 (1)
N1—H1*B*$\cdots$O21($1-x,-1/2+y,2-z$)	2.759 (1)	1.047 (1)	1.725 (1)	168.89 (6)
	2.776 (1)	1.032	1.761 (1)	166.7 (1)
N1—H1*C*$\cdots$O2($2-x,1/2+y,3-z$)	2.837 (1)	1.034 (1)	1.848 (1)	158.72 (3)
	2.859 (1)	1.032	1.867 (1)	159.9 (1)
N1—H1*A*$\cdots$O13	2.939 (1)	1.023 (1)	2.038 (1)	145.45 (5)
	2.945 (1)	1.032	2.030 (1)	146.3 (1)
C6—H6$\cdots$O22($x,y+1,z$)	3.210 (1)	1.082 (1)	2.135 (1)	172.20 (5)
	3.224 (1)	1.077	2.165 (1)	173.0 (1)
C8—H8$\cdots$O14	3.325 (2)	1.071 (1)	2.381 (1)	146.28 (4)
	3.371 (1)	1.077	2.407 (1)	145.4 (1)

distances of 2.41–2.44 Å. In LHP, the O13$\cdots$O12 distance is equivalent (within the estimated standard uncertainty) to the O$\cdots$O distance observed in a neutron study of the paraelectric phase of the ammonium dihydrogen phosphate (ADP) [d(O$\cdots$O) = 2.471 (4) Å] (Pérès *et al.*, 1997). In this last case, two sites separated by 0.377 (5) Å appear for the proton, indicating either a static or a dynamic disorder in the H-atom position. In LHP, no evidence of a symmetric bond or of a proton transfer between O13 and O12 atoms is observed. The most significantly correlated effect is the long O—H distance of 1.059 (1) Å, almost 0.09 Å longer than the average distance observed from neutron diffraction data (Allen *et al.*, 1992).

4.2. Molecular vibration analysis

TLS refinements were carried out using all XR-B, XL-Nb, NR-A and NR-B models (Table 5). In all cases, the molecular vibrations derived from the **T**, **L** tensors agree well with the hydrogen-bonding pattern. For the phosphate anion, the **T** eigenvector associated with the largest eigenvalue is nearly parallel to **a** (the angle ranges from 4.9 to 7.7°) and, therefore, directed perpendicular to the $H_3PO_4\cdot H_2PO_4^-$ layers, where the strongest hydrogen-bond interactions are concentrated. In the case of phosphoric acid, the corresponding eigenvector tends to align along **b** (the angle ranging from 17.5 to 31.1°), as this molecule does not present any interaction along this direction. Another example of the hydrogen-bonding effect on the molecular vibrations is the nearly parallel eigenvectors associated with the smallest eigenvalues of the **T** tensors corresponding to H_3PO_4 and $H_2PO_4^-$ (12.4 or 28.6°, depending on the pair of molecules considered, for XL-Nb).

In order to compare the molecular vibrations at different temperatures, the normal modes of the molecular vibrations were calculated. These modes were obtained from the diagonalization of the 6×6 matrix **W** (Willis & Pryor, 1975):

$$\mathbf{W}=\mathbf{M}^{1/2}\begin{pmatrix}\mathbf{T} & \mathbf{S}^T\\ \mathbf{S} & \mathbf{L}\end{pmatrix}\mathbf{M}^{1/2}, \qquad (4)$$

where **M** is a six-element vector, whose first three components are equal to the mass of the molecule and the last three to its inertial moments. In this expression, the **T**, **L** and **S** tensors are expressed in the inertial coordinate system.

The eigenvectors of **W** provide a decomposition of the molecular vibrations in six independent movements combining translation and libration with amplitudes defined by the corresponding eigenvalues (W). From the amplitudes, the frequency associated with each normal mode can be calculated (Cyvin, 1968; Bürgi, 1995) solving numerically:

$$W=\frac{h}{2\pi\nu}\coth\left(\frac{h\nu}{kT}\right), \qquad (5)$$

where h and k are respectively the Planck and Boltzmann constants and ν is the frequency of the mode. The decomposition in normal modes, defined by the **W** eigenvectors and the corresponding frequencies, provides a temperature-independent description of the molecular vibrations, allowing for a better comparison between TLS models at different temperatures.

In Fig. 5, the normal-mode frequencies for all LHP moieties and TLS refinements are represented. As shown, the agreement between the XL-Nb, XR-A and NR-A results is good, leading to a similar molecular vibrations description for the three models, independently of the different temperatures. In the case of histidine, only five modes are shown, as one of the eigenvalues of W for this molecule is very close to zero and slightly negative. The only significant differences appear for NL-B (the values, not shown on Fig. 5, are given in the supplementary material), where some modes exhibit frequency values which do not agree with the other models. This behaviour is certainly due to the low quality of the NL data set, which required additional *DIFABS* corrections.

4.3. Topological analysis of the electron-density distribution in hydrogen-bond regions

In order to analyse the effect of the refinement strategy on the modelling of the electron density in hydrogen bonds, the topology of $\rho(\mathbf{r})$ was studied in internuclear H$\cdots X$ (X = C, N, O) regions. Within the framework of the Atoms in Molecules theory (Bader, 1990), interatomic interactions are characterized by the topological and energetic properties of $\rho(\mathbf{r})$ at the

Table 5
T and **L** tensor eigenvalues for several TLS refinements.

Standard uncertainties of the eigenvalues were estimated by error propagation on the multiplication of the **T** and **L** tensors including s.u.'s by their eigenvectors without s.u.'s.

		L (rad^2 10^4)			**T** (Å^2 10^4)			$\langle\varphi\rangle$ (rad^2)
XR-A	Phosphate	199 (8)	63 (6)	23 (6)	287 (4)	180 (4)	112 (3)	
	Phosphoric acid	146 (5)	72 (5)	44 (5)	309 (3)	223 (2)	131 (2)	
	Histidinium	36 (9)	14 (2)	0 (3)	245 (14)	179 (12)	148 (2)	79 (11)
XL-Nb	Phosphate	98 (4)	30 (3)	13 (3)	137 (1)	87 (2)	55 (1)	
	Phosphoric acid	71 (3)	32 (3)	24 (3)	150 (2)	104 (1)	64 (1)	
	Histidinium	17 (5)	6 (1)	0 (1)	125 (8)	97 (7)	88 (4)	36 (6)
NR-A	Phosphate	195 (7)	56 (8)	27 (8)	265 (7)	159 (7)	93 (5)	
	Phosphoric acid	144 (5)	74 (6)	42 (6)	282 (6)	192 (5)	106 (4)	
	Histidinium	39 (9)	14 (2)	0 (3)	222 (14)	162 (12)	109 (7)	74 (13)
NL-B	Phosphate	79 (2)	24 (3)	14 (2)	124 (2)	102 (3)	83 (2)	
	Phosphoric acid	59 (5)	27 (6)	19 (6)	146 (6)	112 (5)	88 (4)	
	Histidinium	14 (4)	6 (1)	0 (1)	125 (7)	107 (7)	91 (3)	31 (6)

bond critical points (BCP's): the electron density $\rho_{\rm CP}$, the Laplacian of the electron density $\nabla^2\rho_{\rm CP}$ (which is the Hessian trace), the curvatures of the distribution ($\lambda_{1,\rm CP}$, $\lambda_{2,\rm CP} < 0$ and $\lambda_{3,\rm CP} > 0$, which are the Hessian eigenvalues) and the local electron kinetic, potential and total energy densities at BCP's ($G_{\rm CP}$, $V_{\rm CP}$ and $H_{\rm CP}$, respectively).

The experimental analysis of $\rho(\mathbf{r})$ permits the characterization of the BCP topological properties of the electron distribution but not the energetic ones. For closed-shell interactions, it has been shown (Espinosa *et al.*, 1998, 2001) that $G_{\rm CP}$, $V_{\rm CP}$ (and therefore $H_{\rm CP} = G_{\rm CP} + V_{\rm CP}$) can be estimated from the topological properties by using Abramov's functional for $G_{\rm CP}$ (Abramov, 1997):

$$G_{\rm CP} = \tfrac{3}{10}(3\pi^2)^{2/3}\rho_{\rm CP}^{5/3} + \tfrac{1}{6}\nabla^2\rho_{CP} \qquad (6)$$

and the local form of the virial theorem:

$$V_{CP} = \tfrac{1}{4}\nabla^2\rho_{\rm CP} - 2G_{\rm CP}. \qquad (7)$$

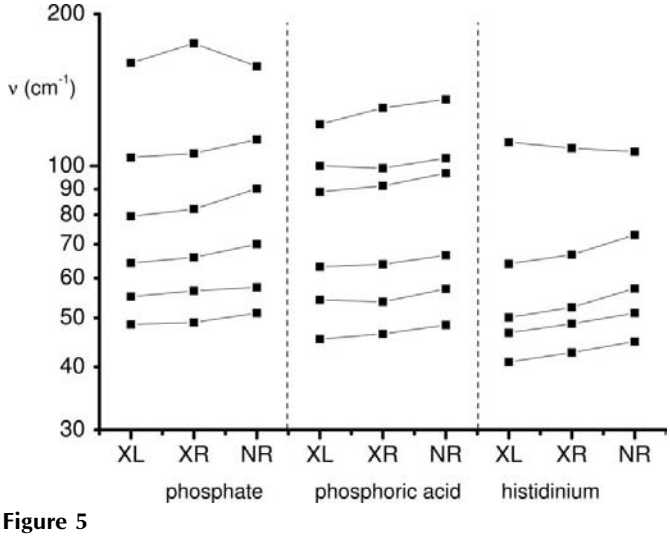

Figure 5
Normal-mode frequencies for the three LHP moieties obtained from XL, XR and NR.

According to a theoretical study involving $X{-}{\rm H}\cdots{\rm F}{-}Y$ systems (Espinosa *et al.*, 2002), both $\nabla^2\rho_{\rm CP}$ and the total electron energy density $H_{\rm CP}$ (or, equivalently, the ratio $|V_{\rm CP}|/G_{\rm CP}$) are indicators of the closed- or shared-shell character of the atomic pairwise interaction. From this theoretical analysis, all the topological and energetic properties show a continuous dependence with the hydrogen-acceptor distance. Associated with the values of these indicators, the complete range of distances can be divided into three regions, corresponding to three different types of interactions. For large distances, $\nabla^2\rho_{\rm CP} > 0$ and $H_{\rm CP} > 0$ as the contribution of the local kinetic energy is in excess in the interaction region ($|V_{\rm CP}|/G_{\rm CP} < 1$), thus indicating a pure closed-shell interaction. For short distances, $\nabla^2\rho_{\rm CP} < 0$ and $H_{\rm CP} < 0$, *i.e.* the potential energy is now in large excess ($|V_{\rm CP}|/G_{\rm CP} > 2$) and the interaction is shared-shell (covalent bond). The intermediate region, corresponding to the transition between these kinds of interaction, is characterized by $\nabla^2\rho_{\rm CP} > 0$ and $H_{\rm CP} < 0$ ($1 < |V_{\rm CP}|/G_{\rm CP} < 2$). In this intermediate region, the population of the bonding orbital grows very fast as the distance decreases due to the actual formation of the incipient covalent bond. Here, although the interaction remains mainly closed shell (the electron-density distribution is still locally depleted, as indicated by the positive value of $\nabla^2\rho_{CP}$), it presents a shared-shell character owing to the excess of $V_{\rm CP}$ compared to $G_{\rm CP}$ ($H_{\rm CP} < 0$).

Shared- and closed-shell interatomic interactions can thus be analysed by the local energy densities at the BCP, which can be estimated from the topological properties of $\rho(\mathbf{r})$. The topological aspects of the distribution are in turn determined by the morphology of $\rho(\mathbf{r})$, as shown in Fig. 6 for LHP. There, the XL-Na (dipole and quadrupole fit for H atoms), XL-Nb (dipole fit only), XL-Nc (dipole and constrained quadrupole fit for H atoms) and XL-A (X–X model) total static electron-density distributions are very similar around all the atoms except H atoms, as a result of their different modelling. In hydrogen-bonding regions, similar characteristics are observed in the four distributions, which however exhibit differences in the electron-density magnitudes, depending on the refinement type. The dipole-only XL-Nb and XL-A

refinements are very similar, and exhibit lower electron-density values than the other two, with differences that can be as large as 0.10 e $Å^{-3}$ (Fig. 7). Also in the case of XL-Nb and XL-A, the total electron density is flatter in the direction perpendicular to the hydrogen bond. In XL-Nc, the electron-density distribution observed in the hydrogen-bonding regions is in general close to that of XL-Na.

The main differences between the models shown in Fig. 6 involve the treatment of quadrupolar parameters in the multipolar expansion of the H atoms. The use of structural information obtained from neutron data has little effect on the electron-density distribution in the bonding region, as seen in Fig. 7(*a*), where models XL-A and XL-Nb are compared. Significant variations between these models are only observed around the nuclear positions owing to slight differences in the coordinates and in the thermal parameters. On the other side, the observed differences between the XL-Na and XL-Nb models show the effect of the quadrupolar term in the modelling of the H atoms, increasing the electron density along the axis of the covalent bond and in the hydrogen-bonding region. Thus, as shown in Fig. 7(*b*), XL-Na presents a larger electron density at both sides of the H atoms along the bond directions. In the hydrogen-bonding region, ρ(XL-Na) is greater than ρ(XL-Nb) by 0.10–0.15 e $Å^{-3}$, which is 2–3 times larger than the calculated standard uncertainty of the electron density (§3.2.3). Nevertheless, the differences shown in Fig.

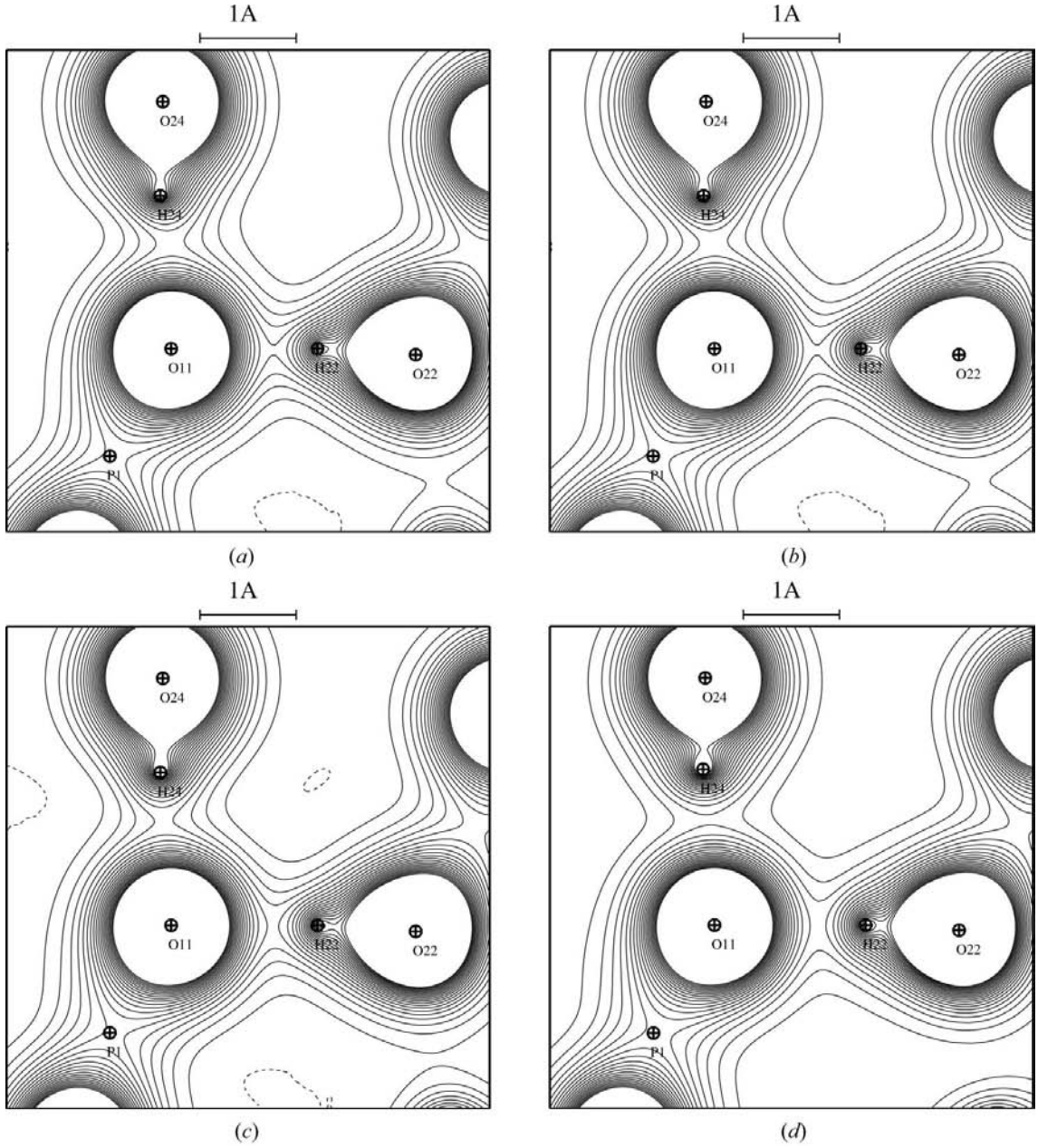

Figure 6
Static total electron density in the plane defined by O11, H22 and H24(1−*x*, −1/2+*y*, 1−*z*) for (*a*) XL-Na, (*b*) XL-Nb, (*c*) XL-Nc and (*d*) XL-A refinements. Contour intervals are 0.10 e $Å^{-3}$.

7(*b*) would be significant when compared to the corresponding residual maps (given in the supplementary material), which are almost identical for the four models and only present random noise of ~ 0.05 e Å^{-3} in the hydrogen-bonding regions.

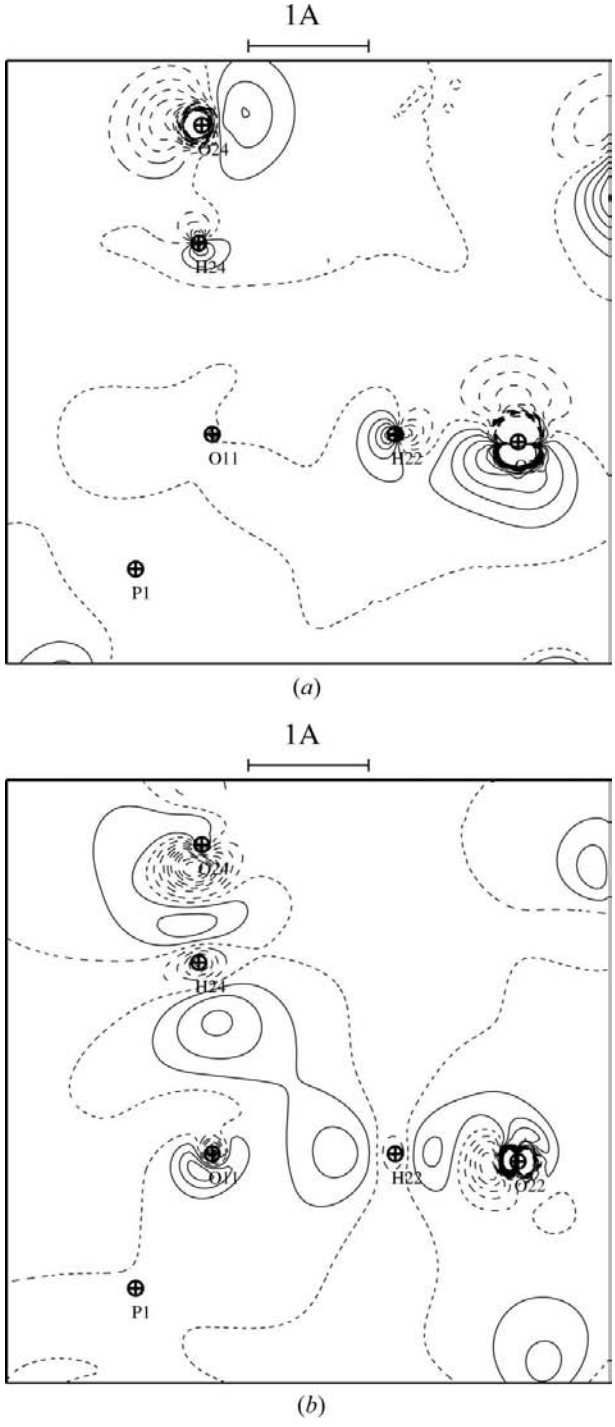

Figure 7
Electron-density difference between models in the same plane as in Fig. 6: (*a*) $\Delta\rho = \rho$(XL-Nb) $- \rho$(XL-A) and (*b*) $\Delta\rho = \rho$(XL-Na) $- \rho$(XL-Nb). Contour intervals are 0.05 e Å^{-3}. Solid and broken lines represent positive and negative contours, respectively. The zero contour is represented by dotted lines.

The $\rho(\mathbf{r})$ topological properties at the BCP's of the X—H$\cdots$O (X = C, N, O) hydrogen bonds observed in LHP were calculated for the multipolar models obtained from XL-Na,

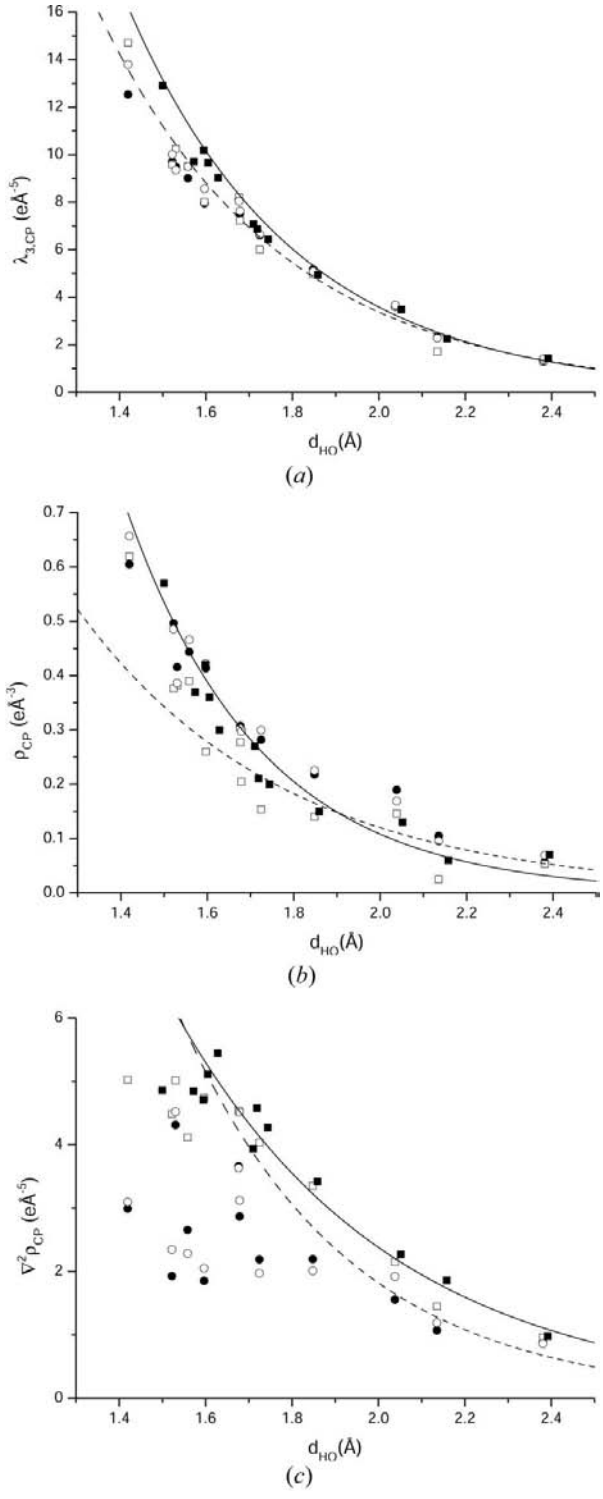

Figure 8
Topological properties at the BCP's of the hydrogen bonds observed in LHP *versus* H$\cdots$O distance. Open circles correspond to XL-Na, squares to XL-Nb, filled circles to XL-Nc and filled squares to XL-A. The curves correspond to the empirical dependences by Espinosa, Souhassou *et al.* (1999) [solid for X–X and dashed for X–N and X–(X+N) refinements].

Table 6
Sums of residuals $\left[\sum(\rho_{CP,mod} - \rho_{CP,cal})^2\right]^{1/2}$, where $\rho_{CP,mod}$ and $\rho_{CP,cal}$ refer to the electron density at BCP calculated from one of the LHP models (XL-Na, XL-Nb, XL-Nc or XL-A) and from one of the empirical curves [X–X or X–(X+N)] of Espinosa, Souhassou *et al.* (1999), respectively; units are e Å^{-3}.

	Empirical curves	
Model	X–X	X–(X+N)
XL-Na	0.160	0.370
XL-Nb	0.282	0.268
XL-Nc	0.155	0.401
XL-A	0.130	0.299

XL-Nb, XL-Nc and XL-A refinements with the *NewProp* program (Souhassou & Blessing, 1999; Souhassou, 1999). For the four models, the calculated magnitudes of ρ_{CP}, $\nabla^2\rho_{CP}$ and $\lambda_{3,CP}$ are represented against the internuclear $d_{H\cdots O}$ distance in Fig. 8.

According to the theoretical analysis of X—H$\cdots$F—Y interactions (Espinosa *et al.*, 2002), topological properties of pure closed-shell interactions are expected to decay exponentially with the $d_{H\cdots A}$ distance, a result that was also observed from the experimental analysis of the 83 X—H$\cdots$O interactions (Espinosa, Souhassou *et al.*, 1999). In this last work, exponential dependences were found separately for 62 hydrogen bonds with $1.561 < d_{H\cdots O} < 2.608$ Å in ten experimental electron-density distributions determined by X–X refinements (solid lines in Fig. 8), and for 21 hydrogen bonds with $1.570 < d_{H\cdots O} < 2.634$ Å in five electron-density distributions from X–N and X–(X+N) refinements (dashed lines in Fig. 8).

For the four refinements, the calculated values of the curvature along the bond path $\lambda_{3,CP}$ agree well with both empirical curves, which are very close to each other (Fig. 8*a*). Nevertheless, in the case of ρ_{CP}, while both curves are very similar for $d_{H\cdots O} > 1.6$ Å, they separate from each other for $d_{H\cdots O} < 1.6$ Å, outside the range used for their derivation. The crystal structure of LHP presents five interactions with $d_{H\cdots O} < 1.6$ Å. For the XL-Na, XL-Nc and XL-A models, the ρ_{CP} values calculated for these interactions agree better with the X–X curve, as shown in Fig. 8(*b*) and in Table 6 from the residual sums. This suggest that the X–X curve provides a good estimation for distances below 1.6 Å. According to the theoretical results on the F$\cdots$H interaction (Espinosa *et al.*, 2002), an important change in the dependence of ρ_{CP} on $d_{H\cdots O}$ is not expected in the early stages of the transition from closed- to shared-shell interactions. Thus, a single exponential would be able to fit both long and intermediate ranges of interaction distances. Although the experimental dependences were derived only for long-range interactions, the LHP results show that the X–X curve seems to provide a good estimation also for the intermediate range.

The $\nabla^2\rho_{CP}$ values are smaller in XL-Na and XL-Nc than in XL-Nb and XL-A for all interactions, indicating the main effect of the quadrupolar term in the modelling of the H atoms on this topological property. Furthermore, the XL-Nb and XL-A values agree well with the empirical curves, which are close to each other for $d_{H\cdots O} > 1.561$ Å. For shorter distances than $d_{H\cdots O} \approx 1.65$ Å, the $\nabla^2\rho_{CP}$ magnitudes fall below the exponential curve due to the incipient formation of the bonding molecular orbital, which gives rise to the covalent bond (where $\nabla^2\rho_{CP} < 0$) at approximately $d_{H\cdots O} < 1.33$ Å (Espinosa *et al.*, 1998).

For XL-Na and XL-Nc, the $\nabla^2\rho_{CP}$ values do not show any trend as a function of $d_{H\cdots O}$. The low $\nabla^2\rho_{CP}$ values for these refinements are related to larger values of the negative curvatures perpendicular to the hydrogen-bond path. Indeed, the H-atom quadrupolar terms ($m = 1$ in XL-Na and $m = 0$ in XL-Nc) tend to increase the electron-density magnitude at the hydrogen-bond BCP, but this contribution is concentrated along the bond axis, as seen in Figs. 6 and 7, thus increasing $\lambda_{1,CP}$ and $\lambda_{2,CP}$ and decreasing $\nabla^2\rho_{CP}$.

This model-dependent behaviour of the topological properties has important consequences on the analysis of the local

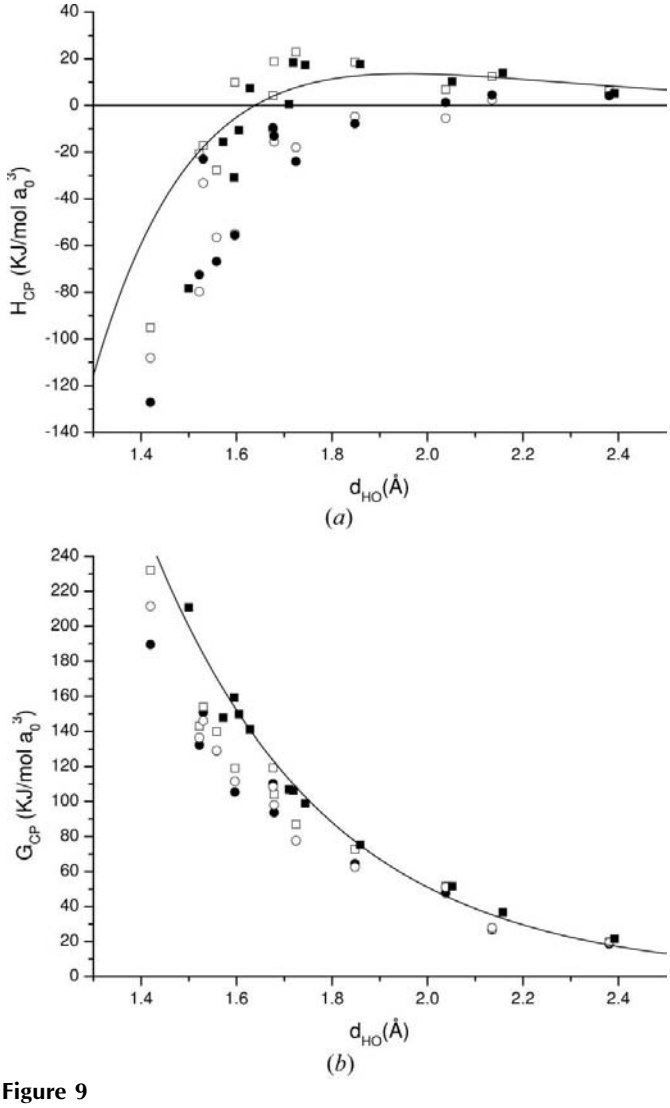

Figure 9
Energetic properties at the BCP's of the hydrogen bonds observed in LHP *versus* H$\cdots$O distance. Symbols are defined as in Fig. 8. The curves are the empirical dependences from Espinosa *et al.* (1998) and Espinosa & Molins (2000).

energy densities at BCP. In Fig. 9(*a*), the values of H_{CP} for the four refinements are presented along with the empirical dependence derived from applying equations (6) and (7) to the set of 83 hydrogen bonds (Espinosa *et al.*, 1998; Espinosa & Molins, 2000). According to this empirical dependence, pure closed-shell ($H_{CP} > 0$) interactions are found only for $d_{H\cdots O} > 1.640$ Å. For LHP, this means that the five N—H$\cdots$O and the two C—H$\cdots$O interactions are of pure closed-shell type, whereas the five strong O—H$\cdots$O bonds are not. The only difference between the behaviour expected from the empirical dependence and the results of XL-Nb and XL-A appears for the longest O—H$\cdots$O interaction, which presents $H_{CP} > 0$ in the experimental topology. On the other hand, for XL-Na and XL-Nc, only the two ($d_{H\cdots O} > 2.1$ Å) and the three ($d_{H\cdots O} > 2.0$ Å) weakest interactions, respectively, can be considered as pure closed-shell type. In addition, for the XL-Nb and XL-A models, the observed H$\cdots$O distance where the $\nabla^2\rho_{CP}$ exponential dependence is abandoned ($d_{H\cdots O} \approx 1.65$ Å) is in agreement with the distance $d_{H\cdots O} = 1.640$ Å, related to $H_{CP} = 0$, which is the energetic condition associated with the change in the dependence of $\nabla^2\rho_{CP}$ observed in the closed-shell region (Espinosa *et al.*, 2002).

The particular behaviour of H_{CP} in XL-Na and XL-Nc is related to that of V_{CP}, as G_{CP} values are similar for the four refinements and agree quite well with the empirical curve (Fig. 9*b*). According to the empirical dependences, G_{CP} and V_{CP} are proportional to the curvatures parallel ($\lambda_{3,CP}$) and perpendicular ($\lambda_{1,CP}$ and $\lambda_{2,CP}$) to the bond-path direction, respectively (Espinosa, Lecomte & Molins, 1999). Thus, larger values of $\lambda_{1,CP}$ and $\lambda_{2,CP}$ in XL-Na and XL-Nc are related to higher V_{CP} magnitudes, and therefore to the observed behaviour of H_{CP} for these refinements, which exhibit lower total energy-density values.

Among the three models including neutron data, XL-Nb is the closest to XL-A. For both of them, the multipolar expansion carried out for the H atoms was extended up to the dipolar term. These models show similar agreements with the empirical dependencies of the topological and energetic properties, and larger differences between their topological properties are up to 0.05 e Å^{-3} for ρ_{CP} (H1*B*$\cdots$O21), 1.0 e Å^{-5} for $\nabla^2\rho_{CP}$ (H23$\cdots$O12) and 1.8 e Å^{-5} for $\lambda_{3,CP}$ (H13$\cdots$O12). As far as the use of neutron-derived positions for the H atoms in XL-Nb leads to longer *X*—H bond distances, and therefore to shorter H$\cdots$O interactions, than in XL-Na, the main differences between the two models come from the almost systematic offset of XL-Nb data towards shorter $d_{H\cdots O}$ distances.

5. Conclusions

Depending on the maximum multipolar expansion term of the H atoms, important changes are observed in the topological and energetic properties of the hydrogen-bonding interactions. If the expansion is extended up to the dipolar term, a very good agreement with the empirical dependences given by Espinosa *et al.* (1998) and Espinosa, Souhassou *et al.*, 1999) is observed for the eight H$\cdots$O interactions showing $d_{H\cdots O}$ distances within the same range of values used in the derivation of the empirical curves. For the four H$\cdots$O interactions that exhibit shorter $d_{H\cdots O}$ distances than those belonging to that range, the Laplacian falls below the empirical curve. This is an anticipated result, as the exponential dependence should be abandoned for $H_{CP} < 0$, *i.e.* for $d_{H\cdots O} < 1.640$ Å according to Espinosa & Molins (2000), and the expected behaviour of $\nabla^2\rho_{CP}$ (Espinosa *et al.*, 2002) should reach a local maximum for distances slightly shorter than $d_{H\cdots O} \approx 1.64$ Å, followed by a monotonic decrease up to zero at the border of the shared-shell region, $d_{H\cdots O} < 1.33$ Å (Espinosa *et al.*, 1998), outside the considered range of distances.

On the other hand, larger differences with the empirical dependences appear when quadrupolar terms are included for the modelling of the H atoms, as these terms were not present in most of the pseudoatom models used in the derivation of those empirical dependences. The quadrupoles of the H atoms sharpen the electron-density distribution in the plane orthogonal to the H$\cdots$*A* hydrogen-bond direction, increasing the perpendicular curvatures and therefore decreasing the Laplacian magnitude at the BCP. As all the energetic properties at the BCP are experimentally derived from topological ρ_{CP} and $\nabla^2\rho_{CP}$ data, hydrogen-bond interactions that are found as pure closed shell ($H_{CP} > 0$) in the refinements undertaken without quadrupolar terms present a significant shared-shell character ($H_{CP} < 0$) when these terms are included. As a consequence, results coming from the models that describe the H atoms up to dipolar terms appear to be in better agreement with theoretical calculations (Espinosa *et al.*, 2002). Moreover, it should be noted that the effect of the low-quality ADP's derived from neutron data could bias this analysis because of the correlation between ADP's and quadrupolar terms in the refinement, leading to the concomitant influence on the $\nabla^2\rho_{CP}$ and H_{CP} values.

The use of structural information that has been derived from neutron data for the H atoms does not affect the agreement with the empirical dependences if the multipolar expansion for these atoms is extended up to the dipolar term only. For LHP, the use of this information leads to an almost systematic decrease of the $d_{H\cdots O}$ distances with respect to those observed from X-ray data, which is accompanied in most cases by small variations of the topological properties at the corresponding BCP's.

The experimental electron-density distribution derived from the X-ray low-temperature data set has been used to obtain accurate ADP's from the room-temperature X-ray data. This procedure permits us to obtain unbiased ADP's from the aspherical electron-density contribution when the multipolar refinement cannot be undertaken. Furthermore, the quality of the thermal parameters is better than the one obtained from high-order data only, as low-order reflections are not removed in the refinement and the amount of data is larger. Therefore, the use of generalized scattering factors obtained from low-temperature refinements appears to be a useful tool for improving the quality of ADP's at higher temperatures where multipolar refinements are not feasible.

From the molecular vibration analysis performed with different sets of ADP, it can be seen that the normal-mode decomposition of rigid-body vibrations is useful for comparing molecular vibrations at different temperatures. However, normal modes are very sensitive to systematic errors and the comparison is only possible when high-quality sets of ADP's, free from experimental errors and corrected for the electron-density asphericity, are available.

The authors thank Dr Mohammed Souhassou for his help in the topological analysis. EE thanks Professor R. Guilard for supporting the development of part of this work in the laboratory LIMSAG (Université de Bourgogne, France).

References

Abramov, Y. A. (1997). *Acta Cryst.* A**53**, 264–272.
Allen, F. H., Kennard, O., Watson, D. G., Brummer, L., Orpen, A. G. & Taylor, R. (1992). *International Tables for Crystallography*, Vol. C, edited by A. J. C. Wilson, pp. 685–706. Dordrecht: Kluwer Academic Publishers.
Bader, R. F. W. (1990). *Atoms in Molecules – a Quantum Theory.* Oxford: Clarendon Press.
Becker, P. J. & Coppens, P. (1974). *Acta Cryst.* A**30**, 129–147.
Blessing, R. H. (1986). *Acta Cryst.* B**42**, 613–621.
Blessing, R. H. (1987). *Crystallogr. Rev.* **1**, 3–58.
Blessing, R. H. (1989). *J. Appl. Cryst.* **22**, 396–397.
Blessing, R. H. (1995*a*). *Acta Cryst.* A**51**, 33–38.
Blessing, R. H. (1995*b*). *Acta Cryst.* B**51**, 816–823.
Bürgi, H. B. (1989). *Acta Cryst.* B**45**, 383–390.
Bürgi, H. B. (1995). *Acta Cryst.* B**51**, 571–579.
Chandler, G. S. & Spackman, M. A. (1982). *Acta Cryst.* A**38**, 225–239.
Clementi, E. & Roetti, C. (1974). *At. Data Nucl. Data Tables*, **14**, 177–478.
Coppens, P. (1968). *Acta Cryst.* B**24**, 1272–1274.
Coppens, P. (1970). *Thermal Neutron Diffraction*, edited by B. T. M. Willis, pp. 82–100. Oxford University Press.
Coppens, P., Boehme, R., Price, P. F. & Stevens, E. D. (1981). *Acta Cryst.* A**37**, 857–863.
Creagh, D. C. & McAuley, W. J. (1992). *International Tables for Crystallography*, Vol. C, edited by A. J. C. Wilson, pp. 206–222. Dordrecht: Kluwer Academic Publishers.
Cruickshank, D. W. J. (1949). *Acta Cryst.* **2**, 65–82.
Cyvin, S. J. (1968). *Molecule Vibrations and Mean Square Amplitudes.* Universitats Forlaget and Elsevier, Amsterdam.
DeTitta, G. T. (1985). *J. Appl. Cryst.* **18**, 75–79.
Doyle, P. A. & Cowley, J. M. (1974). *International Tables for X-ray Crystallography*, Vol. IV, pp. 152–175. Birmingham: Kynoch Press.
Dunitz, J. D., Schomaker, V. & Trueblood, K. N. (1988). *J. Phys. Chem.* **92**, 856–867.
Eimerl, D., Velsko, S., Davis, L., Wang, F., Loiacono, G. & Kennedy, G. (1989). *IEEE J. Quant. Electron.* **25**, 179–193.
Espinosa, E. (1994). PhD thesis, Universitat de Barcelona, Spain.
Espinosa, E., Alkorta, I., Elguero, J. & Molins, E. (2002). *J. Chem. Phys.* **117**, 5529–5542.
Espinosa, E., Alkorta, I., Rozas, I., Elguero, J. & Molins, E. (2001). *Chem. Phys. Lett.* **336**, 457–461.
Espinosa, E., Lecomte, C. & Molins, E. (1999). *Chem. Phys. Lett.* **300**, 745–748.
Espinosa, E., Lecomte, C., Molins, E., Veintemillas, S., Cousson, A. & Paulus, W. (1996). *Acta Cryst.* B**52**, 519–534.
Espinosa, E. & Molins, E. (2000). *J. Chem. Phys.* **113**, 5686–5694.
Espinosa, E., Molins, E. & Lecomte, C. (1998). *Chem. Phys. Lett.* **285**, 170–173.
Espinosa, E., Souhassou, M., Lachekar, H. & Lecomte, C. (1999). *Acta Cryst.* B**55**, 563–572.
Farrugia, L. J. (1997). *J. Appl. Cryst.* **30**, 565.
Flensburg, C., Larsen, S. & Stewart, R. F. (1995). *J. Phys. Chem.* **99**, 10130–10141.
Guillot, B., Viry, L., Lecomte, C. & Jelsch, C. (2001). *J. Appl. Cryst.* **34**, 214–223.
Hansen, N. K. & Coppens, P. (1978). *Acta Cryst.* A**34**, 909–921.
Hirshfeld, F. L. (1976). *Acta Cryst.* A**32**, 239–244.
Jelsch, C., Teeter, M. M., Lamzin, V., Pichon-Pesme, V., Blessing, R. H. & Lecomte, C. (2000). *Proc. Natl Acad. Sci. USA*, **97**, 3171–3176.
Johnson, C. K. (1965). *ORTEP-I*. Report ORNL-3794. Oak Ridge Laboratory, Oak Ridge, TN, USA.
Koritsanszky, T. S. & Coppens, P. (2001). *Chem. Rev.* **101**, 1583–1628.
Kuhs, W. F. (1983). *Acta Cryst.* A**39**, 148–159.
Kuntzinger, S., Dahaoui, S., Ghermani, N. E., Lecomte, C. & Howard, J. A. K. (1999). *Acta Cryst.* B**55**, 867–881.
Kurki-Suonio, K. (1977). *Isr. J. Chem.* **16**, 115–123.
Lecomte, C., Aubert, E., Legrand, V., Porcher, F., Pillet, S., Guillot, B. & Jelsch, C. (2005). *Z. Kristallogr.* **220**, 373–384.
McCandlish, L. E., Stout, G. H. & Andrews, L. C. (1975). *Acta Cryst.* A**31**, 245–249.
Madsen, D., Flensburg, C. & Larsen, S. (1998). *J. Phys. Chem. A*, **102**, 2177–2188.
Masse, R. & Zyss, J. (1991). *Mol. Eng.* **1**, 141–152.
Moss, G. R., Souhassou, M., Blessing, R. H., Espinosa, E. & Lecomte, C. (1995). *Acta Cryst.* B**51**, 650–660.
Pérès, N., Boukhris, A., Souhassou, M., Gavoille, G. & Lecomte, C. (1999). *Acta Cryst.* A**55**, 1038–1048.
Pérès, N., Souhassou, M., Wyncke, B., Gavoille, G., Cousson, A. & Paulus, W. (1997). *J. Phys. Condens. Matter*, **9**, 6555–6562.
Pichon-Pesme, V., Lecomte, C. & Lachekar, H. (1995). *J. Phys. Chem.* **99**, 6242–6250.
Puig-Molina, A., Alvarez-Larena, A., Piniella, J. F., Howard, S. T. & Baert, F. (1998). *Struct. Chem.* **9**, 395–402.
Rosenfield, R. E., Demartin, F. & Gramaccioli, C. M. (1978). *Acta Cryst.* A**34**, 828–829.
Ruysink, A. F. J. & Vos, A. (1974). *Acta Cryst.* A**30**, 503–506.
Schomaker, V. & Trueblood, K. N. (1968). *Acta Cryst.* B**24**, 63–76.
Schomaker, V. & Trueblood, K. N. (1998). *Acta Cryst.* B**54**, 507–514.
Sears, V. F. (1992). *Neutron News*, **3**, 26–37.
Souhassou, M. (1999). *NewProp: Computer Program to Calculate the Topological Properties of Electron Density*. CNRS ESA 7036, Université Henri Poincaré, Nancy, France.
Souhassou, M. & Blessing, R. H. (1999). *J. Appl. Cryst.* **32**, 210–217.
Souhassou, M., Espinosa, E., Lecomte, C. & Blessing, R. (1995). *Acta Cryst.* B**51**, 661–668.
Stewart, R. F. (1976). *Acta Cryst.* A**32**, 565–574.
Stewart, R. F., Davidson, E. R. & Simpson, W. T. (1965). *J. Chem. Phys.* **42**, 3175–3187.
Trueblood, K. & Dunitz, J. (1983). *Acta Cryst.* B**39**, 120–133.
Walker, N. & Stuart, D. (1983). *Acta Cryst.* A**39**, 158–166.
Willis, B. T. M. & Pryor, A. W. (1975). *Thermal Vibrations in Crystallography*. Cambridge University Press.
Yokotani, A., Sasaki, T. & Nakai, S. (1989). *Appl. Phys. Lett.* **55**, 2692–2693.